Quantum magnetotransport properties of a MoS_2 monolayer

M. Tahir,[1,*] P. Vasilopoulos,[1,†] and F. M. Peeters[2,‡]
[1]*Department of Physics, Concordia University, Montreal, Quebec, Canada H3G 1M8*
[2]*Departement Fysica, Universiteit Antwerpen Groenenborgerlaan 171, B-2020 Antwerpen, Belgium*
(Received 30 June 2015; published 5 January 2016)

We study transport properties of a MoS_2 monolayer in the presence of a perpendicular magnetic field B. We derive and discuss its band structure and take into account spin and valley Zeeman effects. Compared to a conventional two-dimensional electron gas, these effects lead to new quantum Hall plateaus and new peaks in the longitudinal resistivity as functions of the magnetic field. The field B leads to a significant enhancement of the spin splitting in the conduction band, to a beating of the Shubnikov–de Haas (SdH) oscillations in the low-field regime, and to their splitting in the high-field regime. The Zeeman fields suppress significantly the beating of the SdH oscillations in the low-field regime and strongly enhance their splitting at high fields. The spin and valley polarizations show a similar beating pattern at low fields and are clearly separated at high fields in which they attain a value higher than 90%.

DOI: 10.1103/PhysRevB.93.035406

I. INTRODUCTION

Recent developments in the experimental realization of two-dimensional (2D) transition-metal dichalcogenides MX_2 (M = Mo, W; X = S, Se) have drawn much attention due to potential applications [1–10]. MoS_2 is a semiconducting material with strong spin-orbit splitting $2\lambda' = 150$ meV and a large intrinsic band gap $2\Delta = 1.66$ eV. These properties of MX_2 contrast sharply with those of graphene, the first stable 2D material with promising technological applications in various fields [11], which has a negligible band gap and a very weak spin-orbit coupling (SOC). MoS_2 has the honeycomb structure of graphene but provides a mass to the Dirac fermions [5,6,10]. As a consequence, preliminary results indicate a high potential for valleytronics because the dispersion can be manipulated in a flexible manner for optoelectronic applications [6–9]. Spin and valley Hall effects have been predicted in an experimentally accessible temperature regime [5], the former arising from the strong SOC and the latter from the broken inversion symmetry. Some experimental results for MoS_2 and WSe_2 [7,8,12,13] suggest that monolayers of MX_2 could be used for integrated valleytronic devices. From a fundamental point of view, many efforts have focused on different properties of MoS_2 and other group-VI dichalcogenides in the absence of a magnetic field. To see the effects of such a field and the corresponding Landau levels (LLs), magnetoptical properties [14–16] have been theoretically studied.

The integer quantum Hall effect (QHE) of a 2D electron gas (2DEG)is epitomized by steps in the Hall conductivity of height $2(n+1)e^2/h$ where h is the Planck constant, e the electron charge, and n an integer, and the vanishing of the longitudinal conductivity (dissipationless current) at these steps. In graphene [17–19], the QHE plateaus appear at $4(n+1/2)e^2/h$ and the fourfold degeneracy is associated with the spin and valley degrees of freedom. More recently, the QHE has been assessed for silicene/germanene [20,21] in which the SOC rearranges the LLs in two groups and the plateaus appear at $2(n+1/2)e^2/h$ due to the valley degeneracy except for the $n=0$ LL in which the fourfold degeneracy is lifted. Quantum transport measurements to observe the QHE and Shubnikov–de Haas oscillations (SdH) in high mobility MoS_2 have been performed very recently [22]. Although an unconventional QHE [23] has been predicted for MoS_2 through its band structure, we are aware only of the limited study of ballistic transport in Ref. [24], i.e., in the absence of scattering, but not of any detailed magnetotransport studies that take scattering into account. As clearly stated in Ref. [24], though, trigonal warping contributes a Zeeman-type term to the valley splitting but does not affect much the band structure which depends strongly on the linear term in the magnetic field B [see Sec. II after Eq. (3)].

In this work, we study quantum magnetotransport through a monolayer MoS_2. We derive and discuss the corresponding band structure in the presence of a perpendicular magnetic field and include the spin and valley Zeeman terms. The study of transport is based on general conductivity expressions, derived within the linear-response theory [25], and cast explicitly in terms of single-particle eigenstates and eigenvalues. Using them, we investigate the influence of a magnetic field on the spin and valley Hall conductivity, and show that the plateaus exhibit an unusual sequence. In addition, we evaluate the longitudinal conductivity, and compare the results with those for graphene and silicene or germanene.

The paper is organized as follows. In Sec. II, we present the one-electron eigenstates, eigenvalues, and the corresponding density of states (DOS). In Sec. III, we evaluate the Hall and longitudinal conductivities and discuss our numerical results. Summary and concluding remarks follow in Sec. IV.

II. BASIC MODEL FORMULATION

We consider MoS_2 in the (x,y) plane in a perpendicular magnetic field B. Including two Zeeman terms in the one-electron Hamiltonian of Ref. [5] [Eq. (3)], we obtain

$$H = v_F(\eta\sigma_x\Pi_x + \sigma_y\Pi_y) + (\Delta - \lambda\eta s)\sigma_z + \lambda\eta s + s\mathrm{M}_z - \eta\mathrm{M}_v. \quad (1)$$

*m.tahir06@alumni.imperial.ac.uk
†p.vasilopoulos@concordia.ca
‡francois.peeters@uantwerpen.be

Here, $\eta = \pm 1$ for valleys K and K', $2\Delta \approx 1.66$ eV is the mass term which breaks the inversion symmetry and creates an intrinsic direct band gap, σ_x, σ_y, and σ_z are the Pauli matrices, $\Pi = \mathbf{p}+e\mathbf{A}$ is the 2D canonical momentum with $\mathbf{A}$ the vector potential, v_F denotes the Fermi velocity, and $\lambda = \lambda'/2 = 37.5$ meV is the SOC strength with spin up and spin down represented by $s = +1$ and -1, respectively. Further, $\mathrm{M}_z = g'\mu_B B/2$ is the Zeeman exchange field induced by ferromagnetic order, g' the Landé g factor ($g' = g'_e + g'_s$), and μ_B the Bohr magneton [26]. Also, $g'_e = 2$ is the free-electron g factor and $g'_s = 0.21$ is the out-of-plane factor due to the strong SOC in $\mathrm{MoS_2}$. The last term, $\mathrm{M}_v = g'_v \mu_B B/2$, breaks the valley symmetry of the levels and $g'_v = 3.57$ [26]. The Zeeman field energy has been measured in very recent experiments [27–30] and is theoretically shown to be approximately 30 meV by first-principles calculations [31].

Using the Landau gauge for the vector potential $\mathbf{A} = (0,Bx,0)$ and diagonalizing the Hamiltonian (1), we obtain the eigenvalues

$$E^{\eta,s}_{n,p} = \eta s\lambda + s\mathrm{M}_z - \eta \mathrm{M}_v + pE^{\eta,s}_n,\ E^{\eta,s}_n = \left[n\hbar^2\omega_c^2 + \Delta^2_{\eta s}\right]^{1/2}; \quad (2)$$

here, $\Delta_{\eta s} = \Delta - \eta s\lambda$, $p = +\,(-)$ denotes the electron (hole) states, $\omega_c = v_F\sqrt{2eB/\hbar}$ is the cyclotron frequency, and the integer n labels the Landau levels (LLs). A simpler expression for the eigenvalues is obtained by noticing that $\hbar\omega_c \ll \Delta_{\eta s}$. Expanding the square root gives

$$E^{\eta,s}_{n,p} \approx (1-p)\eta s\lambda + s\mathrm{M}_z - \eta\mathrm{M}_v + p\Delta + pn\,\frac{\hbar^2\omega_c^2}{2\Delta_{\eta s}}. \quad (3)$$

This is a usual, linear in n and B, LL spectrum. Notice that in the conduction band the first term in Eq. (3) vanishes, whereas in the valence band it does not. Using $\Delta \gg \eta s\lambda$, the last term is equal $pn(\hbar^2\omega_c^2/2\Delta)(1+\eta\lambda)$. This gives a spin slitting $E(s=1) - E(s=-1) = 2\mathrm{M}_z + n\eta\lambda(\hbar^2\omega_c^2/\Delta)$ in the conduction band and $2\eta\lambda - n\eta\lambda(\hbar^2\omega_c^2/\Delta)$ in the valence band. The term $n(\hbar^2\omega_c^2/2\Delta) \propto nB$ is about twice as big as M_z and much smaller than λ. It is important in the conduction band but negligible in the valence band in which $\lambda \approx 150$ meV.

The eigenfunctions for the K valley are

$$\Psi^{\eta,s}_{p,n} = \frac{e^{ik_y y}}{\sqrt{L_y}}\begin{pmatrix} \eta\, A^{\eta,s}_{n,p}\,\phi_n \\ B^{\eta,s}_{n,p}\,\phi_{n-1}\end{pmatrix}, \quad (4)$$

where $A^{\eta,s}_{n,p} = [(pE^{\eta,s}_n + \Delta_{\eta s})/2pE^{\eta,s}_n]^{1/2}$, $B^{\eta,s}_{n,p} = [(pE^{\eta,s}_n - \Delta_{\eta s})/2pE^{\eta,s}_n]^{1/2}$, and ϕ_n is the harmonic oscillator function. The eigenfunctions for the K' valley ($\eta = -1$) are obtained from Eq. (4) by exchanging ϕ_n with ϕ_{n-1}. The eigenvalues and eigenfunctions of the $n = 0$ LL are

$$E^{+,s}_0 = \Delta + s\mathrm{M}_z - \mathrm{M}_v, \quad \Psi^{+,s}_{p,0} = \begin{pmatrix}\phi_0\\ 0\end{pmatrix}, \quad (5)$$

$$E^{-,s}_0 = -(\Delta - s\mathrm{M}_z - \mathrm{M}_v + 2s\lambda),\ \Psi^{-,s}_{p,0} = \begin{pmatrix}0\\ \phi_0\end{pmatrix}. \quad (6)$$

For a better appreciation of the spectrum given above, one can contrast it with that for $B = 0$ given by

$$E^{s,\eta}_p = s\eta\lambda + p[v^2\hbar^2k^2 + (\Delta - \lambda\eta s)^2]^{1/2}. \quad (7)$$

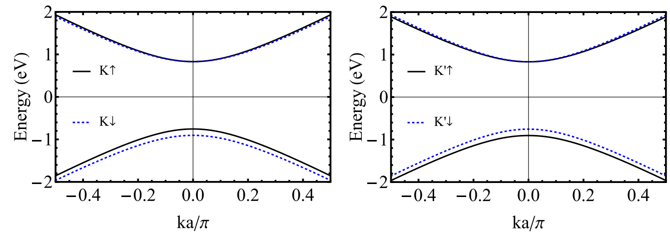

FIG. 1. Band structure of $\mathrm{MoS_2}$ in the absence of a magnetic field B. The left panel is for the K valley and the right one for the K' valley.

Here, $p = 1\ (-1)$ denotes the conduction (valence) band, $s = 1\ (-1)$ is for spin up (down), and $\eta = 1\ (-1)$ for the $K\ (K')$ valley. Further, k is the 2D wave vector. This spectrum (7) is shown in Fig. 1 versus ka where $a = 0.319$ nm is the lattice constant.

We present the eigenvalues given by Eqs. (2), as functions of the magnetic field B in Fig. 2. The top and bottom panels correspond to the conduction and valence bands, respectively, for finite spin M_z and valley M_v Zeeman fields. We find the following: (i) in contrast to the $\sqrt{B}$ dependence in graphene or silicene, the energies of the LLs grow linearly with B. This is obvious from Eq. (3) which holds well because $\hbar\omega_c \ll \Delta_{\eta s}$. (ii) For $\mathrm{M}_z = \mathrm{M}_v = 0$ the spin splitting in the conduction band comes entirely from the last term in Eq. (3). It is approximately twice as big as the M_z term and depends linearly on the LL index n and field B: for $n = 5$ is 1 meV at $B = 10$ T and 2 meV at $B = 20$ T. (iii) As Fig. 2 shows, the energies of the spin-up (-down) LLs at the K valley are different than those

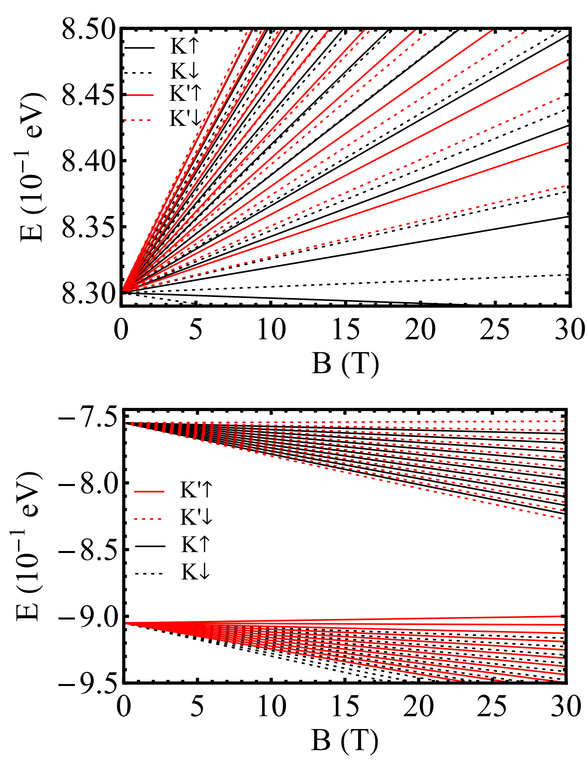

FIG. 2. Band structure of $\mathrm{MoS_2}$ versus magnetic field B including spin and valley Zeeman fields. The top panel is for the conduction band and the bottom one for the valence band.

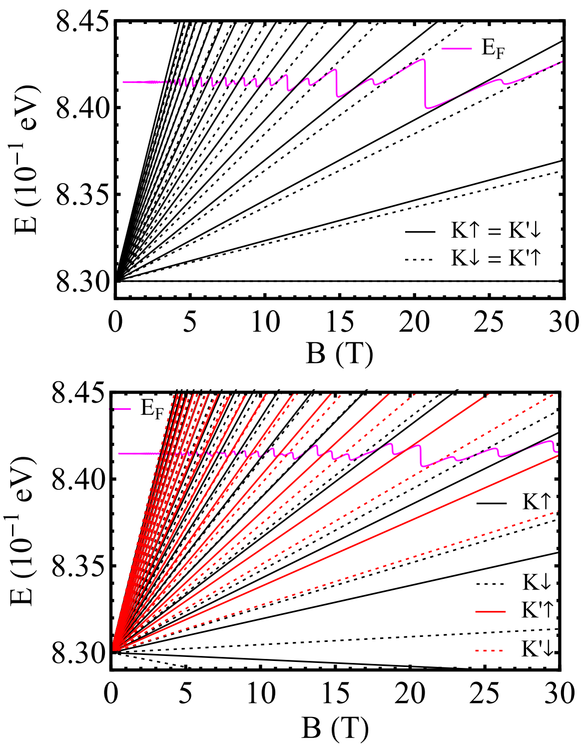

FIG. 3. Landau levels in MoS_2 (conduction band) as functions of the magnetic field B. The top panel is for $M_z = M_v = 0$ and the bottom one for $M_z \neq 0$ and $M_v \neq 0$. The magenta curve shows the Fermi level vs B.

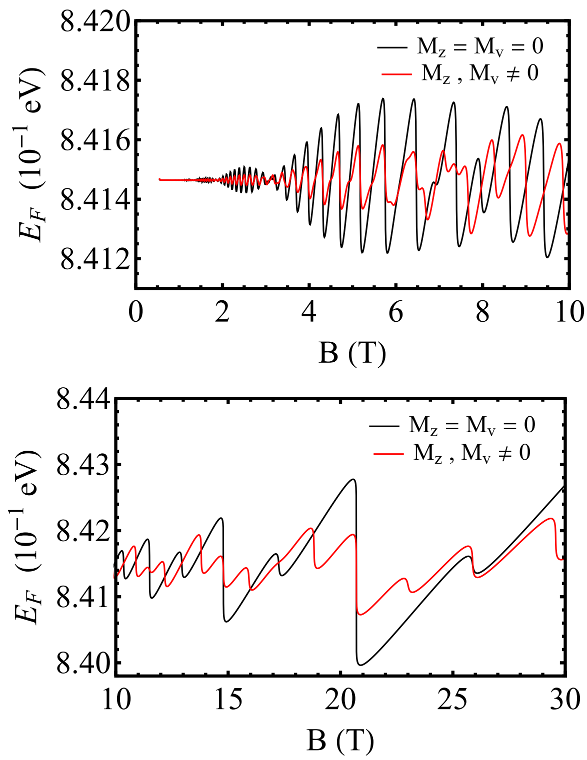

FIG. 4. Fermi level of MoS_2 as a function of perpendicular magnetic field B at $T = 1$ K. The upper and lower panels differ only in the field range (x axis).

of the spin down (up) at the $K^{'}$ valley and show a spin and valley polarization in contrast with the zero magnetic field limit in which they are the same [5]. (iv) For $M_z \neq 0$ and $M_v = 0$ the spin splitting in the conduction band for $n = 5$ is 2.2 meV at $B = 10$ T and 4.3 meV at $B = 20$ T, respectively. (v) In contrast to the $B = 0$ case [5], the spin splitting in the conduction band is about 10 meV for $B = 30$ T ($M_z \neq 0$, $M_v \neq 0$) and can become larger by increasing B. A 10-meV spin splitting in the conduction band has been realized in recent experiments [22]. On the other hand, in the valence band the spin splitting is 150 meV and is the same as that for $B = 0$ [5]. (vi) The $n = 0$ LL is spin and valley degenerate for $M_z = M_v = 0$ in the conduction band and spin nondegenerate in the valence band whereas it is spin nondegenerate for $M_z \neq 0$ in the conduction $(\Delta + sM_z - M_v)$ and valence $(\Delta + 2s\lambda - sM_z - M_v)$ bands due to the additional contribution of M_v.

The Fermi energy is obtained from the electron concentration n_c given by

$$n_c = \int_{-\infty}^{\infty} D(E) f(E) dE = \frac{g_{s/v}}{D_0} \sum_{n,\eta,s} f\left(E_{n,p}^{\eta,s}\right), \tag{8}$$

where $D(E)$ is the density of states (DOS), with $D_0 = 2\pi l^2$, and g_s (g_v) is the spin (valley) degeneracy. Further, $f(E_{n,p}^{\eta,s}) = \{1 + \exp[\beta(E_{n,p}^{\eta,s} - E_F)]\}^{-1}$, with $\beta = 1/k_B T$, is the Fermi-Dirac function. We use $g_s = g_v = 1$ due to the lifting of the spin and valley degeneracies. The DOS is given in the Appendix.

The magenta solid curve in Fig. 3 shows the Fermi level, obtained numerically from Eq. (8), as a function of B; the LLs shown are the same as those in Fig. 2, i.e., spin and valley dependent, since the magnetic field lifts the spin and valley degeneracies of the $n \geqslant 1$ LLs. To appreciate the difference between the case $M_z = M_v = 0$, shown in the top panel, and the case $M_z \neq 0$, $M_v \neq 0$, we replot the spectrum in the lower panel of Fig. 3, versus the field B, for M_z and $M_v = 0$. The additional intra-LL small jumps result from the lifting of the spin and valley degeneracies; the solid and dashed curves ($n \geqslant 1$) are, respectively, for spins up and spins down in the K valley, respectively. For the K' valley the spins are reversed, e.g., for $n \geqslant 1$, the spin-up electrons in the K valley have the same energy as the spin-down ones in the K' valley. For $n \geqslant 1$, the fourfold degeneracy, due to spin and valley, of all LLs is lifted while the $n = 0$ LL in the conduction band is valley degenerate. The Fermi level results in Fig. 3 in the presence of M_z, M_v (M_z, $M_v \neq 0$) correspond to the fourfold-nondegenerate LLs. This is also shown separately in Fig. 4 for a clearer understanding. Another worth noticing feature is the beating of the oscillations for B fields up to about 10 T with a giant splitting of the LLs at higher fields due to the spin and valley Zeeman terms. As we show in the following, such a beating pattern also appears in the DOS and other transport quantities.

The DOS is evaluated in the Appendix [see Eq. (A2)]. We show it in Fig. 5 as a function of the magnetic field B for an electron density $n_c = 5 \times 10^{16}$ m^{-2} and a Fermi velocity $v_F = 5.3 \times 10^5$ ms^{-1} [22]. We plot the dimensionless DOS $D(E_F)/D_c$ ($D_c = g_{s/v}/D_0\Gamma\sqrt{2\pi}$) in the top and bottom panels for the conduction band. For low and high fields B we observe a beating pattern and a splitting of the SdH oscillations, respectively. Both are due to the closeness of the frequencies

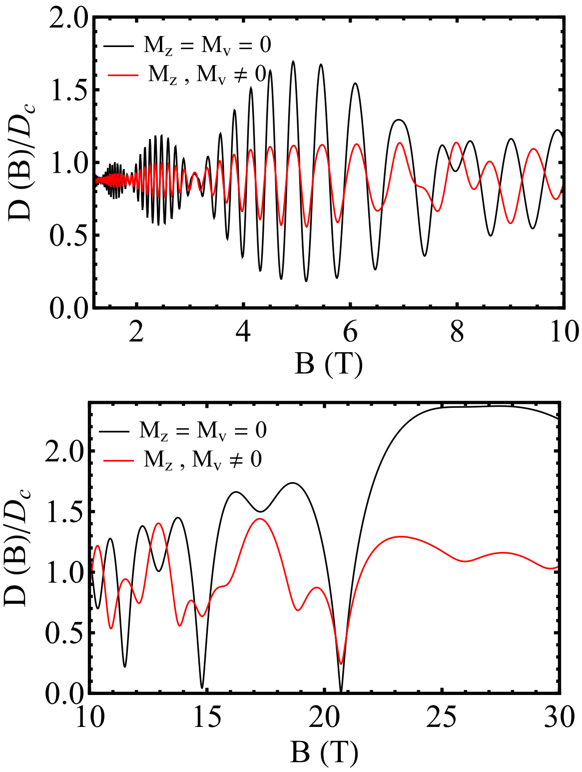

FIG. 5. Dimensionless density of states as a function of perpendicular magnetic field B for a LL width $\Gamma = 0.1\sqrt{B}$ meV. The upper and lower panels differ only in the field range (x axis).

of the spin-up and -down states that result from the splitting of the LLs due to the SOC. The beating is suppressed at very low fields and the splitting of the oscillations becomes more pronounced at high fields. The beating pattern vanishes in the conduction band in the limit $B \to 0$ since so does the SOC splitting in this limit [5].

As shown in Fig. 5, the amplitude is modulated by $\cos(2\pi\delta/\hbar^2\omega_c^2)$ and nodes occur at $\delta/\hbar^2\omega_c^2 = \pm 0.5, \pm 1.5, \ldots$ [see Eq. (A4)]. We also note that the amplitude modulation occurs only when both the SOC and the field B are finite. Further, the threshold magnetic field where beating is seen depends on both λ and Δ.

The beating persists in the conduction band for magnetic fields up to about 10 T. Above this value, it is quenched and the SdH oscillations are split. This behavior is explained by the closeness of the oscillation frequencies of the SOC-split LLs. The magnetic-field-enhanced splitting in the conduction band mixes the spin-up and -down states of neighboring LLs into two unequally spaced energy branches. The beating appears when the subband broadening is of the order of $\hbar\omega_c$. For high magnetic fields, the SOC effects weaken and the beating pattern is replaced by a splitting of the peaks, which persist due to the SOC and Zeeman energies.

The giant splitting of the SdH oscillations in the high-field regime can be understood by the term $\cos[4\pi(G_\eta\Delta + \eta\lambda M_z)/\hbar^2\omega_c^2]$ with and without the Zeeman terms M_z and M_v. Normally this term exhibits SdH oscillations without the terms M_z and M_v; thus, the giant splitting at high fields is purely caused by their presence in the Fermi energy and DOS. Noting that the cyclotron energy is $\hbar\omega_c = 19$ meV at $B = 1$ T, the observation of the LL splitting and the discussed consequences require that the temperature and level broadening are smaller than the splitting due to the SOC.

III. LINEAR-RESPONSE CONDUCTIVITIES

In the linear-response formalism of Ref. [25], the many-body Hamiltonian of the system is written as $H = H_0 + H_I - \mathbf{R} \cdot \mathbf{F}(t)$, where H_0 is the unperturbed part, H_I a binary interaction of electrons, e.g., with impurities or phonons, $-\mathbf{R} \cdot \mathbf{F}(t)$ is the interaction of the system with an external time-dependent field $\mathbf{F}(t)$, $\mathbf{R} = \sum_i \mathbf{r}_i$, and $\mathbf{r}_i$ the position operator of electron i. For electrical transport we have $\mathbf{F}(t) = \tilde{N}e\mathbf{E}(t)$, where $\mathbf{E}(t)$ is the electric field. In the representation in which H_0 is diagonal the many-body density operator $\rho = \rho^d + \rho^{nd}$ has a diagonal (ρ^d) and a nondiagonal (ρ^{nd}) part. Accordingly, the conductivity tensor $\sigma_{\mu\nu}$ has a diagonal ($\sigma^d_{\mu\nu}$) and a nondiagonal ($\sigma^{nd}_{\mu\nu}$) part; the full tensor is $\sigma_{\mu\nu} = \sigma^d_{\mu\nu} + \sigma^{nd}_{\mu\nu}$, $\mu,\nu = x,y$.

A. Longitudinal conductivity, polarizations

In general, two mechanisms contribute to the current, diffusion, and hopping, but usually only one of them is present. When a magnetic field is present, we have only the hopping contribution since the diffusive one, involving only diagonal elements of the velocity operator [25], vanishes. For weak electric fields and weak scattering potentials the longitudinal conductivity $\sigma^d_{xx} \equiv \sigma_{xx}$ due to hopping has the form [25]

$$\sigma_{xx} = \frac{e^2\beta}{2S_0} \sum_{\zeta\zeta'} f(E_\zeta)[1 - f(E_{\zeta'})] W_{\zeta\zeta'} (X_\zeta - X_{\zeta'})^2, \tag{9}$$

with $f(E_\zeta) = f(E^{\eta,s}_{n,p})$ and $S_0 = L_x L_y$ the area of the sample. Further, $W_{\zeta\zeta'}$ is the transition rate between the one-electron states $|\zeta\rangle$ and $|\zeta'\rangle$ and e the charge of the electron. For elastic scattering, we have $f(E_\zeta) = f(E_{\zeta'})$ and conduction occurs by hopping between the orbit centers X_ζ and $X_{\zeta'}$, with $X_\zeta = \langle\zeta|X|\zeta\rangle = \ell^2 k_y$.

At very low temperatures, the dominant scattering mechanism is that of electrons scattered by charged impurities in similar, graphenelike systems (see Ref. [32] for more details). We model the impurity potential as that of a screened charge $U(\mathbf{r}) = (e^2/4\pi\varepsilon_r\varepsilon_0 r)e^{-k_s r}$, where k_s is the screening wave vector, ε_r the relative permittivity, and ε_0 the permittivity of the vacuum. The Fourier transform of $U(\mathbf{r})$ is then given by $U(\mathbf{q}) = U_0/(q^2 + k_s^2)^{1/2}$, with $U_0 = e^2/2\varepsilon_r\varepsilon_0$. Further, if the impurity potential is short ranged (of the Dirac δ-function type), one may use the approximation $k_s \gg q$ and obtain $U(\mathbf{q}) \approx U_0/k_s$. The transition rate is given by

$$W_{\zeta\zeta'} = \frac{2\pi n_i}{S_0\hbar} \sum_{\zeta'} |U(\mathbf{q})|^2 |J_{\zeta\zeta'}(u)|^2 \,\delta(E_\zeta - E_{\zeta'}) \delta_{k_y,k'_y+q_y} \tag{10}$$

with $u = l^2(q_x^2 + q_y^2)/2 = l^2q^2/2$ and n_i the impurity density. $J_{\zeta\zeta'}(u) = \langle\zeta|\exp(i\mathbf{q}\cdot\mathbf{r})|\zeta'\rangle$ are the form factors and $|\zeta\rangle \equiv |n,s,\eta,k_y\rangle$. For elastic impurity scattering, we neglect LL mixing, i.e., we take $n = n'$. Further, we note that $\sigma_{xx} = \sigma_{yy}$ and that for $k_s \gg q$ we can ignore the factor q^2 in $U(\mathbf{q})$. We have

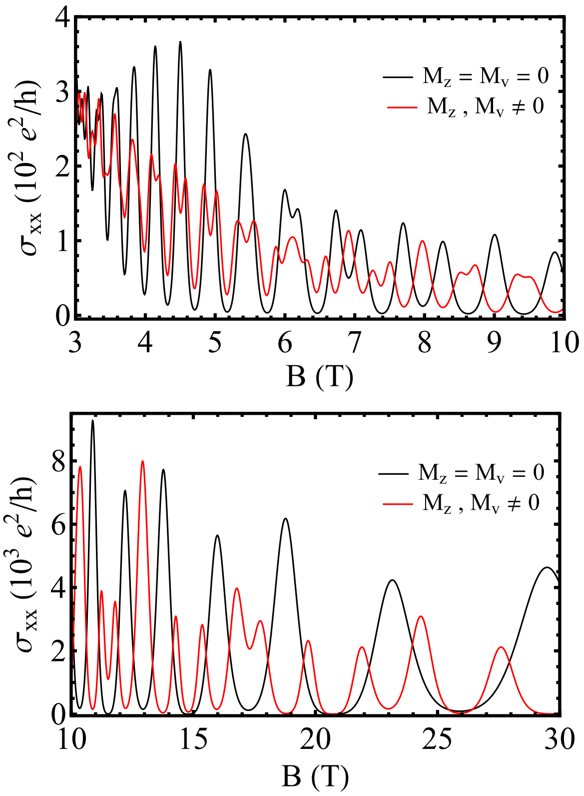

FIG. 6. Longitudinal conductivity as function of magnetic field B for $T = 1$ K. The upper and lower panels differ only in the field range (x axis).

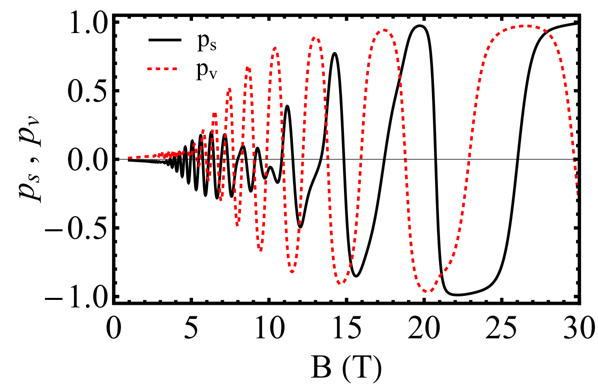

FIG. 7. Spin P_s and valley P_v polarizations versus magnetic field extracted from Eq. (11). The parameters are the same as those pertaining to the $M_z, M_v \neq 0$ curve in Fig. 6.

$(X_\zeta - X_{\zeta'})^2 = l^4 q_y^2$ and $q_y = q \sin\phi$. Since the wave function oscillates around $x_0 = l^2 k_y$ and $0 \leqslant x_0 \leqslant L_x$, the sum over k_y gives a factor $S_0/2\pi l^2$ and that over q is evaluated in cylindrical coordinates. The standard evaluation of $|J_{\zeta\zeta'}(u)|^2$, for $n = n'$, gives $|J_{nn}(u)|^2 = \exp(-u)[|A^{\eta,s}_{n,p}|^2 L_n(u) + |B^{\eta,s}_{n,p}|^2 L_{n-1}(u)]^2$. Further, $\delta(E_\zeta - E_{\zeta'}) = (2\Delta_{\eta s}/\hbar^2\omega_c^2)\delta_{n,n'}$. Inserting these factors in Eq. (9) and evaluating the integral over u, the longitudinal conductivity can be written as

$$\sigma_{xx} = \frac{e^2}{h}\frac{\beta\, n_i U_0^2}{l^2 k_s^2\, \hbar^2\omega_c^2}\sum_{n,s,\eta}\Delta_{\eta s} I_n^{\eta,s} f\big(E^{\eta,s}_{n,p}\big)\big[1 - f\big(E^{\eta,s}_{n,p}\big)\big], \tag{11}$$

where

$$I_n^{\eta,s} = \int_0^\infty u|J_{nn}(u)|^2 du. \tag{12}$$

The integration in Eq. (12) is carried out using the orthogonality of the polynomials $L_n(u)$ and their recurrence relation $(n+1)L_{n+1}(u) - (2n+1-u)L_n(u) + nL_{n-1}(u) = 0$. It gives

$$I_n^{\eta,s} = (2n+1)\big|A^{\eta,s}_{n,p}\big|^4 - 2n\big|A^{\eta,s}_{n,p}\big|^2\big|B^{\eta,s}_{n,p}\big|^2 + (2n-1)\big|B^{\eta,s}_{n,p}\big|^4. \tag{13}$$

As expected, the conductivity obtained from Eq. (11) exhibits SdH oscillations when B is varied. We show that in Fig. 6 for the following parameters [5,22,33]: $n_i = 1 \times 10^{13}$ m^{-2}, $\mu_B = 5.788 \times 10^{-5}$ eV/T, $T = 1$ K, $n_c = 5 \times 10^{16}$ m^2, $k_0 = 1 \times 10^{-7}$ m^{-1}, $v_F = 5.3 \times 10^5$ m/s, and $\epsilon_r = 7.3$ [34]. In contrast with graphene [19] or silicene [21], we find a beating pattern in the SdH oscillations for a B field up to about 8 T and a splitting after this value. Figure 6 shows the SdH oscillations of σ_{xx} for zero (black) and finite (red) Zeeman field energies. For high magnetic fields, the beating pattern disappears and the SdH oscillations are split (see top and bottom panels in Fig. 6). It is a giant splitting and in agreement with the Fermi energy and DOS results shown in Figs. 3–5. The beating pattern is controlled by the magnetic field. It occurs when the subband broadening is of the order of the LL separation $\hbar\omega_c$. For high fields B the SOC effects weaken and the beating pattern is replaced by a splitting of the magnetoconductivity peaks.

The beating pattern can be understood analytically as follows. For very low temperatures, one can make the approximation $\beta f(E^{\eta,s}_{n,p})[1 - f(E^{\eta,s}_{n,p})] \approx \delta(E_F - E^{\eta,s}_{n,p})$, in Eq. (11), broaden the δ function, and carry out the sum over n as outlined in the Appendix. Then, similar to the case of the DOS, the beating pattern is described by the two close-in-frequency cosine terms in Eq. (A3) with the replacement $E \to E_F$. We believe that these results for monolayer MoS_2, and presumably other group-VI dichalcogenides, can be observed by existing experimental techniques [22]. We notice in passing that such a beating pattern, entirely due to the SOC, has been observed experimentally [35] in the conventional 2DEG and treated theoretically [36]. In both cases, the LL spectrum is linear in the field B whereas in graphene or silicene it is proportional to $B^{1/2}$.

Equation (11) contains all spin and valley contributions to the longitudinal conductivity. Extracting them from there one can study the spin P_s and valley P_v polarizations defined by

$$P_s = \frac{\sigma_{xx}^{K,\uparrow} + \sigma_{xx}^{K',\uparrow} - \big(\sigma_{xx}^{K,\downarrow} + \sigma_{xx}^{K',\downarrow}\big)}{\sigma_{xx}^{K,\uparrow} + \sigma_{xx}^{K',\uparrow} + \big(\sigma_{xx}^{K,\downarrow} + \sigma_{xx}^{K',\downarrow}\big)} \tag{14}$$

and

$$P_v = \frac{\sigma_{xx}^{K,\uparrow} + \sigma_{xx}^{K,\downarrow} - \big(\sigma_{xx}^{K',\uparrow} + \sigma_{xx}^{K',\downarrow}\big)}{\sigma_{xx}^{K,\uparrow} + \sigma_{xx}^{K,\downarrow} + \big(\sigma_{xx}^{K',\uparrow} + \sigma_{xx}^{K',\downarrow}\big)}. \tag{15}$$

We plot P_s and P_v versus the field B in Fig. 7; the parameters are the same as those used for producing the red curve in Fig. 6. As expected and can be seen, here too we have beating patterns at relatively low B fields and a clear separation between P_s and P_v at strong fields with both attaining more than 90% above $B = 20$ T.

B. Hall conductivity and magnetoresistivities

Within linear-response theory, the Hall conductivity σ_{yx} is given by [19,25]

$$\sigma^{nd}_{\mu\nu} = \frac{i\hbar e^2}{S_0} \sum_{\zeta\zeta'} \frac{(f_\zeta - f_{\zeta'}) v_{\nu\zeta\zeta'} v_{\mu\zeta'\zeta}}{(E_\zeta - E_{\zeta'})(E_\zeta - E_{\zeta'} + i\Gamma_\zeta)}, \tag{16}$$

where $v_{\nu\zeta\zeta'}\, v_{\mu\zeta'\zeta}$ are the nondiagonal matrix elements of the velocity operator, $\mu,\nu = x,y$, and $S_0 = L_x L_y$. The sums run over all quantum numbers of the states $|\zeta\rangle \equiv |n,s,\eta,k_y\rangle$ and $|\zeta'\rangle \equiv |n',s',\eta',k'_y\rangle$ provided $\zeta \neq \zeta'$. Assuming that the broadening of the LLs is approximately the same for all states, $\Gamma_\zeta = \Gamma$, we find that imaginary part of Eq. (16) vanishes. To obtain the most transparent results for σ_{yx}, we take $\Gamma = 0$.

In MoS_2 there are two inequivalent valleys (K, K') in the Brillouin zone due to the two sublattices and, with finite Zeeman splitting, the fourfold degeneracy is lifted. In the conduction band, this lifting is due to the magnetic field. The matrix elements $\langle\zeta|v_x|\zeta'\rangle$ and $\langle\zeta'|v_y|\zeta\rangle$ can be obtained using the Hamiltonian (1), $v_x = \partial H/\partial p_x$, and $v_y = \partial H/\partial p_y$. We obtain $v_x = \eta v \sigma_x$, $v_y = v\sigma_y$, and, using Eq. (4), the matrix elements

$$\langle\xi|v_x|\xi'\rangle = v\big(A^{\eta,s}_{n,p} B^{\eta',s'}_{n',p'} \delta_{n'-1,n} + B^{\eta,s}_{n,p} A^{\eta',s'}_{n',p'} \delta_{n',n-1}\big), \tag{17}$$

$$\langle\xi'|v_y|\xi\rangle = -\eta i v\big(A^{\eta',s'}_{n',p'} B^{\eta,s}_{n,p} \delta_{n',n-1} - B^{\eta',s'}_{n',p'} A^{\eta,s}_{n,p} \delta_{n'-1,n}\big). \tag{18}$$

For the K' valley n and n' must be interchanged only in the Kronecker deltas.

The matrix elements between the $n = 0$ and the $n \geqslant 1$ LLs are obtained in a similar way. For the K valley the $(n,0)$ matrix elements are

$$\langle\xi|v_x|\xi'\rangle = vA^{\eta,s}_{n,p}\delta_{n-1,0}, \langle\xi'|v_y|\xi\rangle = -ivA^{\eta,s}_{n,p}\delta_{n-1,0}; \tag{19}$$

those for the $(0,n')$ ones are given by Eq. (19) upon changing n' to n and i to $-i$. The results for the K' valley are obtained by replacing $A^{\eta,s}_{n,p}$ with $B^{\eta,s}_{n,p}$.

Since $|\zeta\rangle \equiv |n,s,\eta,k_y\rangle$, there will be one summation over k_y which, with periodic boundary conditions for k_y, gives the factor $S_0/2\pi l^2$. Now, one needs to sum over all possible combinations of the matrix elements and for convenience we write $\sum_{p,p'} = \sum_{+,+} + \sum_{-,-} + \sum_{+,-} + \sum_{-,+}$. Here, the subscript $+/-$ denotes the conduction/valence band and only the $n \geqslant 1$ LLs are considered. The $n = 0$ LL is considered separately. This procedure is detailed in Ref. [19]. The resulting Hall conductivity is $\bar{\sigma}_{yx} = \sigma_{yx} + \Delta\sigma_{yx}$, with

$$\sigma_{yx} = \frac{e^2}{h} \sum_{\eta,s,n=1} (n + 1/2)\big\{f^{\eta,s}_{n,+} - f^{\eta,s}_{n+1,+} + f^{\eta,s}_{n,-} - f^{\eta,s}_{n+1,-}\big\}, \tag{20}$$

$$\Delta\sigma_{yx} = \frac{e^2}{2h} \sum_{\eta,s,n=1} \eta\Delta_{\eta s}\big\{\big(f^{\eta,s}_{n,+} - f^{\eta,s}_{n,-}\big)/E^{\eta,s}_{n,+} - \big(f^{\eta,s}_{n+1,+} - f^{\eta,s}_{n+1,-}\big)/E^{\eta,s}_{n+1,+}\big\}. \tag{21}$$

The sums in Eq. (20) run from $n = 1$ to ∞ and the results for the K and K' valleys are obtained by setting $\eta = +1$ and -1, respectively. Then, writing explicitly the sums over s one sees that the correction terms $\Delta\sigma^K_{yx}$ and $\Delta\sigma^{K'}_{yx}$ cancel each other provided both valleys in the nth LL are occupied; evidently they do not cancel when only one of the spins or valleys is occupied.

The total contribution of the $n = 0$ LL, including both spins and valleys, is

$$\sigma^{0,\eta}_{yx} = \frac{e^2}{h} \sum_{\eta s} \big\{f^{\eta,s}_{0,+} + f^{\eta,s}_{0,-} - \big(f^{\eta,s}_{1,+} + f^{\eta,s}_{1,-}\big)/2 + \big(f^{\eta,s}_{1,+} - f^{\eta,s}_{1,-}\big)\eta\Delta_{\eta s}/2E^{\eta,s}_{1,+}\big\}. \tag{22}$$

Note again that the terms $\eta\Delta_{\eta s}$ cancel each other when summing the valley contributions $\sigma^{0,K}_{yx} + \sigma^{0,K'}_{yx}$, due to the opposite spin states in the two valleys. This reveals that the conductivity σ_{yx} is essentially independent of $\eta\Delta_{\eta s}$; that is, the size of the band gap does not affect the correction terms $\Delta\sigma^K_{yx}$ in the Hall conductivity. This limit agrees with the results for gapped graphene or silicene although MoS_2 and other group-VI dichalcogenides are different from these materials due to a strong SOC, a large intrinsic direct band gap, and an asymmetry between the two bands (for $B = 0$ the spin splitting is 0 and 150 meV in the conduction and valence bands, respectively [5]). In the limit $\lambda \to 0$, these results reduce to similar ones for gapped graphene [26] and for graphene in the limit of $\Delta = \lambda = 0$ [17]. In contrast, for $\Delta,\lambda \neq 0$, as in the case of MoS_2 and other group-VI dichalcogenides, we see a

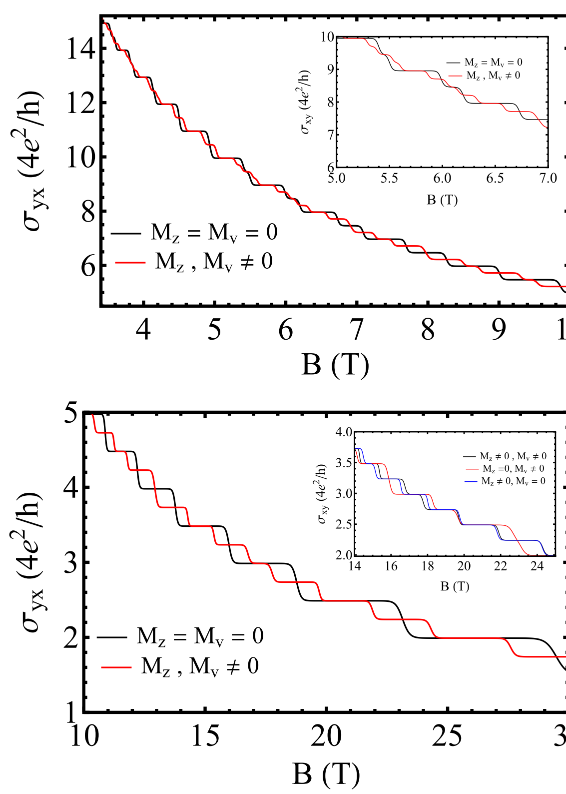

FIG. 8. Hall conductivity as a function of the magnetic field B for $T = 1$ K. The upper and lower panels differ only in the field range (x axis). For further clarity, the range 5–7 T is shown in the inset to the upper panel and the range 14–25 T in that to the lower one. This inset covers the cases $M_z = M_v = 0$, $M_z = 0, M_v \neq 0$, and $M_z \neq 0, M_v = 0$.

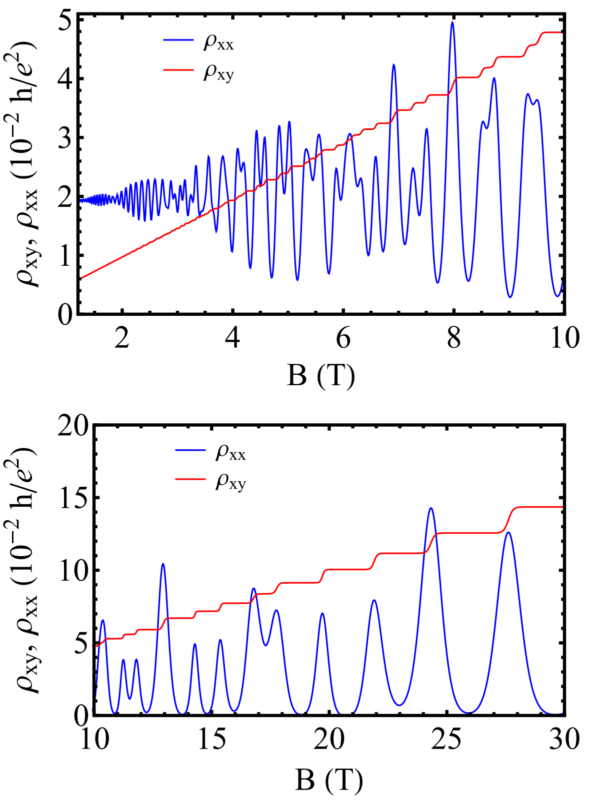

FIG. 9. Longitudinal (blue) and Hall (red) resistivities as functions of the magnetic field B for $T = 1$ K and finite spin and valley Zeeman fields. The upper and lower panels differ only in the field range (x axis); the parameters are the same.

huge gap and splitting due to the SOC in both K,K' valleys as discussed in detail below Eq. (7). As shown in Fig. 8, in addition to the graphene plateaus, that occur at half-integer values of $4e^2/h$, we find plateaus at integer values of $4e^2/h$ as well as at other fractional multiples of $4e^2/h$, e.g., 2.25 and 2.75 due to the spin and valley terms.

At zero or very low temperatures, the last sum in Eqs. (20) and (21) has the value 4 or 2 for $n = n_F$ depending on whether the number of filled spin and valley states is four or two, respectively. The latter occurs when the magnetic field increases the splitting due to the SOC, splits the LLs, and allows intra-LL jumps of E_F between spin and valley states in the same LL (cf. Fig. 3). But, for graphene on a hBN substrate, the gap corresponding to $\Delta - \eta s\lambda$ is constant and the fourfold degeneracy of the LLs makes this sum always equal to 4 because the occupation probability is equal for all spin and valley states. As a result, the additional small jumps of the Fermi level, clearly seen in the curves of Fig. 3, lead to new steps in the Hall conductivity σ_{yx} of MoS_2. In addition, here we have important features for high magnetic fields, the spin- and valley-induced steps due to the Zeeman fields (see insets to Fig. 8).

To compare with experimental results [22], we evaluate the components of the resistivity tensor $\rho_{\mu\nu}$, μ, $\nu = x$, y, from those of the conductivity tensor $\sigma_{\mu\nu}$ using the standard expressions $\rho_{xx} = \sigma_{yy}/S$, $\rho_{yy} = \sigma_{xx}/S$, and $\rho_{xy} = -\sigma_{yx}/S$, where $S = \sigma_{xx}\,\sigma_{yy} - \sigma_{xy}\,\sigma_{yx}$ with $S \approx \sigma_{xy}^2 = n_e^2 e^2/B^2$. The longitudinal and Hall resistivities are shown in Fig. 9 as functions of the magnetic field for temperature $T = 1$ K. The longitudinal resistivity is obtained from the relation $\rho_{xx} = (B/n_c e)^2 \sigma_{xx}$ [19], where n_c is the carrier concentration. We observe extra plateaus in the Hall resistivity due to the SOC and the two Zeeman terms. We find that the steps between the plateaus coincide with sharp peaks in the longitudinal resistivity. In strong magnetic fields, larger than 10 T, we find a significant splitting of the Hall plateaus and the corresponding peaks in the longitudinal resistivity due to the spin and valley Zeeman effects. In contrast, for magnetic fields less than 10 T we observe a beating pattern of the SdH oscillations. It is interesting to note that this pattern is similar to that due to the Rashba SOC in a conventional 2DEG [36]. The predicted SdH oscillations agree well with recent experiments [22] at high magnetic fields. The particular features shown here below 10 T could be tested by more detailed experiments.

IV. SUMMARY AND CONCLUSIONS

We studied quantum magnetotransport properties of a MoS_2 monolayer subject to an external perpendicular magnetic field. At $B = 0$ the spin splitting energy is zero in the conduction and 150 meV in the valence band. We showed though that the magnetic field can enhance it in the conduction band by an amount $\propto nB$ approximately twice as large as M_z [see text after Eq. (3) and Fig. 2]. The combined action of the SOC and of the magnetic and Zeeman fields allows for intra-LL transitions and leads to new quantum Hall plateaus. Moreover, for fields B stronger than 10 T, the peaks of the SdH oscillations of the longitudinal conductivity are doubled whereas for fields below 10 T a beating pattern is observed similar to that of a conventional 2DEG [36]. A similar beating pattern is also exhibited, at low fields, by the spin and valley polarizations. It is also worth emphasizing their oscillations in the entire range of the B field covered and their higher than 90% value for $B \geqslant 20$ T.

The deep minima in the SdH oscillations are accompanied by Fermi level jumps and the peaks coincide with the usual singularities of the DOS. We have shown a beating and splitting of the SdH oscillations in the resistivity, which can be controlled and enhanced by increasing the magnetic field. Indeed, the magnetic field enhances the spin splitting in the conduction band [cf. last term in Eq. (3)], which in turn enhances the splitting and beating of the SdH oscillations. The spin and valley Zeeman fields lead to a giant splitting for strong magnetic fields and the lifting of the fourfold spin and valley degeneracies. We expect that these results will be tested by experiments.

ACKNOWLEDGMENT

This work was supported by the Canadian NSERC Grant No. OGP0121756 (M.T., P.V.) and by the Flemish Science Foundation (FWO-Vl) (F.M.P.).

APPENDIX

The density of states (DOS) is given by $D(E) = (1/S_0)\sum_{n,\eta,s,k_y}\delta(E - E_{n,p}^{\eta,s})$, where $S_0 = L_x L_y$ is the area of the system. The sum over k_y is evaluated using the prescription $(k_0 = L_x/2l^2)$ $\sum_{k_y} \to (L_y g_s g_v/2\pi)\int_{-k_0}^{k_0} dk_y = (S_0/D_0) g_s g_v$, where $D_0 = 2\pi l^2$; g_s and g_v are the spin and valley degeneracies, respectively. We use $g_s = g_v = 1$ due to the lifting of the spin and valley degeneracies. Assuming a Gaussian broadening of the LLs the DOS becomes

$$D(E) = \frac{g_{s/v}}{D_0} \frac{1}{\Gamma\sqrt{2\pi}} \sum_{n,\eta,s} \exp\left[-\left(E - E^{\eta,s}_{n,p}\right)^2/2\Gamma^2\right], \quad \text{(A1)}$$

where $\Gamma = 0.1\sqrt{B}$ meV is the width of the Gaussian distribution [32].

The sum over n is evaluated with the help of the Poisson summation formula [37]. The resulting DOS is

$$D(E) = \sum_{\eta,s} D_1 \left\{1 + 4\sum_{k=1}^{\infty}(-1)^k \cos\left(4\pi k \frac{(G_\eta - s\mathrm{M}_z)\,\Delta_{\eta s}}{\hbar^2\omega_c^2}\right) \times e^{-2(\pi k \Gamma \Delta_{\eta s}/\hbar^2\omega_c^2)^2}\right\}, \quad \text{(A2)}$$

where $D_1 = \Delta_{\eta s}/4\pi v^2\hbar^2$ and $G_\eta = E - \Delta + \eta \mathrm{M}_v$. The first term inside the curly brackets is the monotonic part and the second term the oscillatory part of the DOS. It is sufficient to retain only the term $k = 1$ since the $k > 1$ terms are strongly damped. The oscillatory part leads to a beating pattern at low fields B and a splitting of the SdH oscillations at higher B for $\lambda\Delta \ll E$. The pattern is due to two close-to-each other frequencies due to level splitting and its nodes occur when the summand in Eq. (A2) vanishes. Combining the terms for $s = +1$ and -1 shows that this occurs for

$$\cos\left[4\pi(G_\eta\Delta + \eta\lambda\mathrm{M}_z)/\hbar^2\omega_c^2\right]\cos\left[2\pi\delta/\hbar^2\omega_c^2\right] = 0, \quad \text{(A3)}$$

where $\delta = 2(\eta\lambda G_\eta + \Delta\mathrm{M}_z)$. The nodes of the second cosine term occur for

$$2\pi\delta/\hbar^2\omega_c^2 = (2m+1)\pi/2, m \text{ integer.} \quad \text{(A4)}$$

[1] A. Splendiani, L. Sun, Y. Zhang, T. Li, J. Kim, C. Y. Chim, G. Galli, and F. Wang, Nano Lett. **10**, 1271 (2010).
[2] K. F. Mak, C. Lee, J. Hone, J. Shan, and T. F. Heinz, Phys. Rev. Lett. **105**, 136805 (2010).
[3] B. Radisavljevic, A. Radenovic, J. Brivio, V. Giacometti, and A. Kis, Nat. Nanotechnol. **6**, 147 (2011).
[4] T. Korn, S. Heydrich, M. Hirmer, J. Schmutzler, and C. Schüller, Appl. Phys. Lett. **99**, 102109 (2011).
[5] D. Xiao, G.-B. Liu, W. Feng, X. Xu, and W. Yao, Phys. Rev. Lett. **108**, 196802 (2012).
[6] T. Cao, G. Wang, W. Han, H. Ye, C. Zhu, J. Shi, Q. Niu, P. Tan, E. Wang, B. Liu, and J. Feng, Nat. Commun. **3**, 887 (2012).
[7] K. F. Mak, K. He, J. Shan, and T. F. Heinz, Nat. Nanotechnol. **7**, 494 (2012).
[8] H. Zeng, J. Dai, W. Yao, D. Xiao, and X. Cui, Nat. Nanotechnol. **7**, 490 (2012).
[9] G. Sallen, L. Bouet, X. Marie, G. Wang, C. R. Zhu, W. P. Han, Y. Lu, P. H. Tan, T. Amand, B. L. Liu, and B. Urbaszek, Phys. Rev. B **86**, 081301(R) (2012).
[10] M. Tahir, A. Manchon, and U. Schwingenschlögl, Phys. Rev. B **90**, 125438 (2014).
[11] C. Lee, Q. Li, W. Kalb, X. Z. Liu, H. Berger, R. W. Carpick, and J. Hone, Science **328**, 76 (2010).
[12] S. Wu, J. S. Ross, G.-B. Liu, G. Aivazian, A. Jones, Z. Fei, W. Zhu, D. Xiao, W. Yao, D. Cobden, and X. Xu, Nat. Phys. **9**, 149 (2013).
[13] A. M. Jones, H. Yu, N. J. Ghimire, S. Wu, G. Aivazian, J. S. Ross, B. Zhao, J. Yan, D. G. Mandrus, D. Xiao, W. Yao, and X. Xu, Nat. Nanotechnol. **8**, 634 (2013).
[14] F. Rose, M. O. Goerbig, and F. Piechon, Phys. Rev. B **88**, 125438 (2013).
[15] R.-L. Chu, X. Li, S. Wu, Q. Niu, W. Yao, X. Xu, and C. Zhang, Phys. Rev. B **90**, 045427 (2014).
[16] Y.-H. Ho, Y.-H. Wang, and H.-Y. Chen, Phys. Rev. B **89**, 155316 (2014).
[17] V. P. Gusynin and S. G. Sharapov, Phys. Rev. Lett. **95**, 146801 (2005).
[18] M. Tahir and K. Sabeeh, J. Phys.: Condens. Matter **24**, 135005 (2012).
[19] P. M. Krstajić and P. Vasilopoulos, Phys. Rev. B **86**, 115432 (2012).
[20] M. Tahir and U. Schwingenschlogl, Sci. Rep. **3**, 1075 (2013).
[21] Kh. Shakouri, P. Vasilopoulos, V. Vargiamidis, and F. M. Peeters, Phys. Rev. B **90**, 235423 (2014).
[22] X. Cui, G.-H. Lee, Y. D. Kim, G. Arefe, P. Y. Huang, C.-H. Lee, D. A. Chenet, X. Zhang, L. Wang, F. Ye, F. Pizzocchero, B. S. Jessen, K. Watanabe, T. Taniguchi, D. A. Muller, T. Low, P. Kim, and J. Hone, Nat. Nanotechnol. **10**, 534 (2015).
[23] X. Li, F. Zhang, and Q. Niu, Phys. Rev. Lett. **110**, 066803 (2013).
[24] H. Rostami and R. Asgari, Phys. Rev. B **91**, 075433 (2015).
[25] M. Charbonneau, K. M. Van Vliet, and P. Vasilopoulos, J. Math. Phys. **23**, 318 (1982).
[26] A. Kormányos, V. Zólyomi, N. D. Drummond, and G. Burkard, Phys. Rev. X **4**, 011034 (2014).
[27] D. MacNeill, C. Heikes, K. F. Mak, Z. Anderson, A. Kormnyos, V. Zlyomi, J. Park, and D. C. Ralph, Phys. Rev. Lett. **114**, 037401 (2015).
[28] A. Srivastava, M. Sidler, A. V. Allain, D. S. Lembke, A. Kis, and A. Imamoglu, Nat. Phys. **11**, 141 (2015).
[29] G. Aivazian, Z. Gong, A. M. Jones, R.-L. Chu, J. Yan, D. G. Mandrus, C. Zhang, D. Cobden, W. Yao, and X. Xu, Nat. Phys. **11**, 148 (2015).
[30] Y. Li, J. Ludwig, T. Low, A. Chernikov, X. Cui, G. Arefe, Y. D. Kim, A. M. van der Zande, A. Rigosi, H. M. Hill, S. H. Kim, J. Hone, Z. Li, D. Smirnov, and T. F. Heinz, Phys. Rev. Lett. **113**, 266804 (2014).
[31] Y. C. Cheng, Q. Y. Zhang, and U. Schwingenschlögl, Phys. Rev. B **89**, 155429 (2014).
[32] Y. Zheng and T. Ando, Phys. Rev. B **65**, 245420 (2002); T. Stauber, N. M. R. Peres, and F. Guinea, *ibid.* **76**, 205423 (2007).

[33] A. T. Neal, H. Liu, J. Gu, and P. D. Ye, ACS Nano **7**, 7077 (2013).
[34] B. Radisavljevic and A. Kis, Nat. Mater. **12**, 815 (2013).
[35] J. Luo, H. Munekata, F. F. Fang, and P. J. Stiles, Phys. Rev. B **41**, 7685 (1990).
[36] X. F. Wang and P. Vasilopoulos, Phys. Rev. B **72**, 085344 (2005); **67**, 085313 (2003).
[37] F. M. Peeters, P. Vasilopoulos, and J. Shi, J. Phys.: Condens. Matter **14**, 8803 (2002); V. Yu. Tsaran and S. G. Sharapov, Phys. Rev. B **90**, 205417 (2014).